High-performance electroabsorption modulator*

Zhang Wei(张伟)†, Pan Jiaoqing(潘教青), Zhu Hongliang(朱洪亮), Wang Huan(王桓), and Wang Wei(王圩)

(Key Laboratory of Semiconductor Materials Science, Institute of Semiconductors, Chinese Academy of Sciences, Beijing 100083, China)

Abstract: A 100-μm-long electroabsorption modulator monolithically integrated with passive waveguides at the input and output ports is fabricated through ion implantation induced quantum well intermixing, using only a two-step low-pressure metal–organic vapor phase epitaxial process. An InGaAsP/InGaAsP intra-step quantum well is introduced to the active region to improve the modulation properties. In the experiment high modulation speed and high extinction ratio are obtained simultaneously, the electrical-to-optical frequency response (E/O response) without any load termination reaches to 22 GHz, and extinction ration is as high as 16 dB.

Key words: electroabsorption modulator; quantum well intermixing; intra-step quantum well
DOI: 10.1088/1674-4926/30/9/094008 **EEACC:** 2560

1. Introduction

The electroabsorption modulator (EAM) is a promising transmitter device for use in 40 Gbit/s very-short-reach optical link applications because of its compactness and ease of operation[1, 2]. In order to improve EAM performance, it is necessary to optimize various aspects of the device. The length, width, and layer structure of the active layer are the critical design issues for achieving a wide modulation bandwidth and a high extinction ratio[3] which are generally in a trade-off relation, restricting the overall performance. The modulation bandwidth of a lumped EAM is limited by the RC time constant, so reduction of the capacitance will give rise to a wide modulation bandwidth[4, 5]. The introduction of a traveling-wave electrode will decrease the limitation of the RC time constant, and show promising results[6, 7]. In order to reduce the capacitance, downscaling in waveguide dimensions is used in this letter, such as setting a 3 μm wide, 100 μm long waveguide. This will make the device difficult to handle and package, so it is integrated with a 100 μm long passive waveguide at each side through quantum well intermixing (QWI). An EAM integrated with passive waveguides at the input and output ports is desirable for easy crystal cleavage, low-cost packaging.

For the passive section, QWI is selectively used to make its bandgap blue-shifted from the EAM material to reduce the direct inter-valence band absorption loss[8]. By contrast with butt-joint and selective area growth (SAG) techniques, QWI allows for postgrowth tuning of the QW band edge in a relatively simple procedure and it does not change the average composition, but only slightly changes the compositional profile with a negligible index discontinuity at the interface between adjacent sections. This eliminates parasitic reflections that can degrade performance[9].

An intra-step quantum well (IQW) is proposed to improve the modulation properties. IQW improves the saturation power mainly because the step barrier can delay the onset of the quantum-confined Stark effect (QCSE) to a higher electric field. When the EAM operates under a higher electric field, the photogenerated carriers trapped in wells can easily escape, thereby reducing the screening effect and increasing the saturation power[10]. The IQW has the additional merit of a large QCSE[11–13].

For these reasons, in this study, a novel electroabsorption modulator monolithically integrated with passive waveguides at the input and output port is fabricated through QWI, and IQW is introduced to the active region to improve the modulation properties. High modulation speed and high extinction ratio can be obtained simultaneously. In the experiment an electrical-to-optical frequency response (E/O response) up to 22 GHz without any load termination, and extinction ration as high as 16 dB, are obtained.

2. Device design and fabrication

Figure 1 is a schematic diagram of the device. The 100 μm long EAM was integrated with a 100 μm long passive waveguide at each port. The EAM structure was grown on a (100) semi-insulating InP substrate, using two-step low-pressure metal-organic vapour phase epitaxy (LP-MOCVD). The growth temperature was 650 °C. SiH_4 and DEZn were employed as n- and p-type dopants, respectively.

The first growth process consists of a 0.3 μm thick InP buffer layer, a 1 μm thick n^+-InGaAsP layer, an intrinsic layer, and a 250 μm thick InP space layer. The 1 μm thick n^+-InGaAsP layer forms a single-sided large optical cavity (LOC)

* Project supported by the National High Technology Research and Development Program of China (No. 2006AA01Z256), the State Key Development Program for Basic Research of China (Nos. 2006CB604901, 2006CB604902), and the National Natural Science Foundation of China (No. 90401025).

† Corresponding author. Email: zw2006@semi.ac.cn

Received 12 March 2009, revised manuscript received 22 April 2009 © 2009 Chinese Institute of Electronics

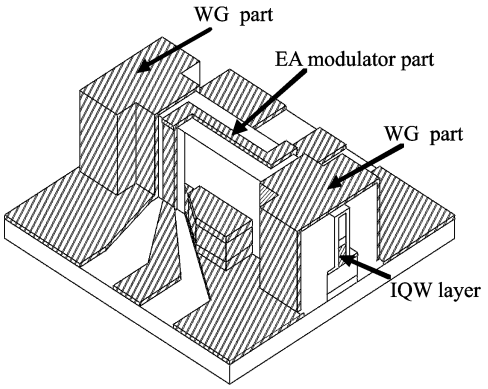

Fig. 1. Schematic diagram of the device structure.

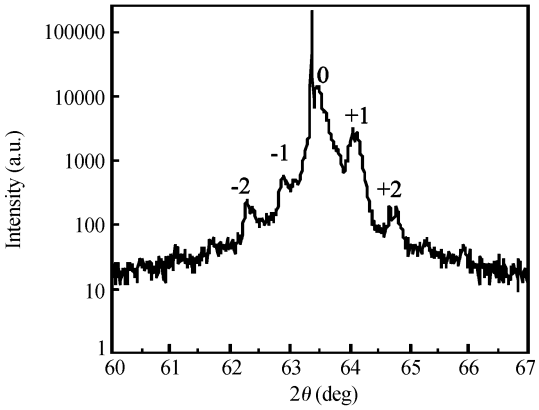

Fig. 2. Measured DCXRD curve of the IQW structure.

structure to reduce the coupling loss with the fibers due to mode-mismatch[14]. The intrinsic layer consists of 10 periods of IQWs, with the tensile strained well, compressively strained intra-step barrier, and barrier, in thicknesses of 8, 6 and 7 nm, respectively. Figure 2 shows the measured DCXRD pattern of the grown InGaAsP/InGaAsP IQW structure; the second- and third-order satellite peaks have a double-peak structure because of the IQW layer[15]. The IQW consists of two common QWs: one was formed by the well and barrier, and the other was formed by the well and intra-step barrier. In the DCXRD test, each QW will produce a set of diffraction patterns which is determined by the QW parameter; if there is difference in periods of the two sets of diffraction patterns, the DCXRD pattern will show a double-peak structure, and the numerical calculation needs more consideration. The IQW layer shows weak tensile strain, which is good for polarization insensitivity[16].

Then the EAM section was capped by a 400 nm thick SiO_2 layer to prevent P^+ ion implantation in the subsequent QWI process. The QWI process involves ion implantation and rapid thermal annealing (RTA). In our experiments, the ion implantation condition is as follows: the energy is 50 keV, the dose is 1×10^{14} cm^{-3}, and the substrate temperature is 200 °C. The RTA condition is 90 s at 700 °C. Figure 3 shows the photoluminescence (PL) spectrum of the samples subjected to 700 °C RTA treatment for various RTA times. The blueshift exhibits a steady increase with anneal time from 60 to 150 s. However, the PL intensity begins to decrease when the anneal

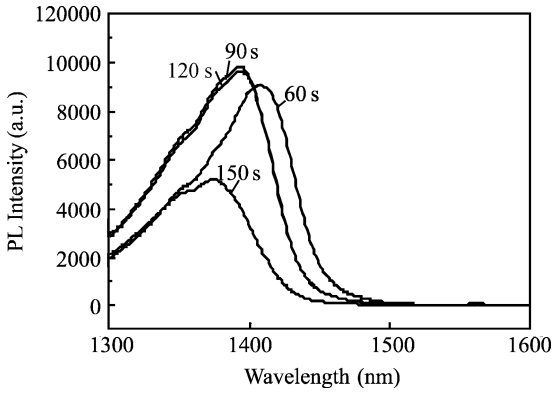

Fig. 3. PL spectra of waveguide section when annealed at 700 °C for different times.

time reaches 90 s. This is why we choose the anneal time as 90 s. After P^+ ion implantation in the waveguide sections, many point defects were generated in the undoped InP space layer and were activated during the subsequent RTA process. The diffusion of the point defects causes the composition intermixing between the well and the barrier. As a result, the peak photoluminescence wavelength of the IQW layer in waveguide sections is blue-shifted from 1498 to 1393 nm, while the bandgap wavelength for the EAM region remains almost unchanged. A 50 nm thick InGaAsP layer, a 50 nm thick InP layer, a 1.8 μm thick p-InP cladding layer and a 0.3 μm thick p-InGaAs cap layer were then grown in the second epitaxial growth step. Then the deep ridge waveguide was fabricated on the wafer by reactive etch (RIE) using the mask of the SiO_2 layer with a 3 μm width. The depth of the ridge is about 2.4 μm. The p-InGaAs layer of the waveguide sections was removed before He^+ ion implantation. Doses of He^+ ions at different energies were carefully chosen to create enough vacancies in the p-InP cladding layer, changing it to a higher resistance material, in order to reduce parallel capacitance of the EAM. Further mesa wet etchings were used to open the n-contact layer and expose the semi-insulation region. Polyimide was then spun, patterned, and cured to smoothen the metal transition between the different material layers and electrical isolation. The CPW electrodes were formed by Ti/Au e-beam evaporation and photolithography. Finally, the devices were lapped and cleaved for testing. This epi-layer process is compatible with other photonic devices to realize a monolithic integrated photonic system as described before.

3. Measurement and discussion

The non-polarized light from a tunable laser diode was taken in and out of the device through tapered lens-fibers. Figure 4 shows the normalized extinction ratio and photocurrent curve as a function of the reverse bias voltage for an optical power of 0 dBm at 1550 nm. The curves are taken without anti-reflection coating on the facets. As shown in Fig. 4, the best modulation efficiency is about 6.9 dB/V from 2 to 3 V and the modulation depth is about 16 dB for the bias from 0 to 4 V. The photocurrent increases as the reverse bias increases.

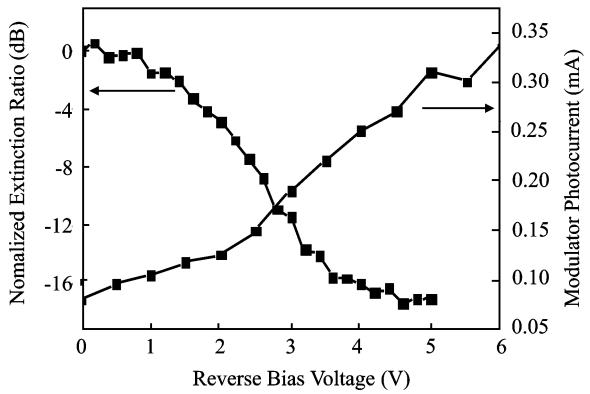

Fig. 4. Normalized extinction ratio and photocurrent curves for 1550 nm incident-light.

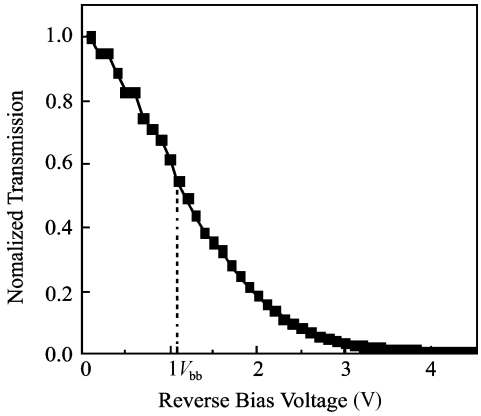

Fig. 5. Normalized transfer curve for 1550 nm incident-light.

Figure 5 shows the normalized transfer curve. The equivalent V_π, defined by Eq. (1)[17], is about 2.3 V. In the function $T_{\rm N}$ is the normalized transfer curve, and $V_{\rm bb}$ is the best bias point for maximum modulation efficiency.

$$V_\pi = \frac{\pi}{2}\left(\frac{\partial T_{\rm N}}{\partial V}\right)^{-1}\Bigg|_{V=V_{\rm bb}}. \tag{1}$$

Figure 6 shows a schematic diagram for the EAM frequency response measurement; a high-speed vector network analyzer (40 GHz, Agilent E8363B) and a broadband photodetector were employed to characterize the microwave properties (S-parameters) and also the high-speed E/O response. The measurement system can only be calibrated up to the two coaxial ports: one is the microwave probe input port (location A), and another is the photodetector output port (location B). The EAM frequency response has to be extracted from the measured S-parameters of the cascaded network, which includes the microwave probe, the EAM and the photodetector. $S_{ij}^{\rm N}$, $S_{ij}^{\rm PR}$, $S_{ij}^{\rm EA}$ and $S_{ij}^{\rm PD}$ are S-parameters for the cascaded network, microwave probe, EAM and photodetector respectively. The objective of the post-measurement extraction is to calculate $S_{21}^{\rm EA}$ from the measured $S_{ij}^{\rm N}$, provided that $S_{ij}^{\rm PR}$ and $S_{ij}^{\rm PD}$ are already known.

$$S_{21}^{\rm EA} = \frac{S_{21}^{\rm N} S_{12}^{\rm PR}}{\left[S_{12}^{\rm PR} S_{21}^{\rm PR} + S_{22}^{\rm PR}\left(S_{11}^{\rm N} - S_{11}^{\rm PR}\right)\right] S_{21}^{\rm PD}}. \tag{2}$$

Equation (2) is the extracted frequency response for the

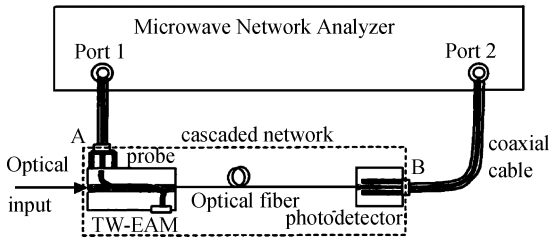

Fig. 6. Schematic diagram showing the measurement of EAM frequency response.

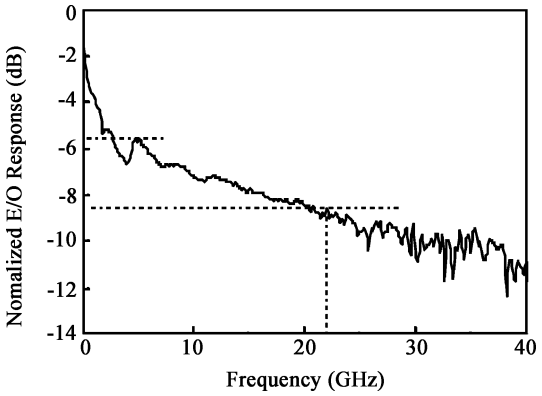

Fig. 7. E/O frequency response of EAM.

EAM[18]; $S_{21}^{\rm PD}$ for the photodetector can come from the manufacturer, and $S_{ij}^{\rm PR}$ of the microwave probe can be extracted from a set of 1-port reflection measurements using on-chip calibration standards (50 Ω-load, open and short). When the probe tip is connected to an on-chip standard, they form a cascaded network similar to that formed by the probe and the EAM. Γ is the measured reflection coefficient for the cascaded network.When we connect the probe to three on-chip standards, we can measure three Γ values (i.e., Γ_1, Γ_2 and Γ_3 for load, open and short standards, respectively), therefore we get three independent equations, which are enough to solve the three unknowns $S_{11}^{\rm PR}$, $S_{22}^{\rm PR}$, $S_{12}^{\rm PR}$ ($S_{12}^{\rm PR} = S_{21}^{\rm PR}$ for a reciprocal network). The final solution is:

$$S_{11}^{\rm PR} = \Gamma_1, \tag{3}$$

$$S_{22}^{\rm PR} = \frac{\Gamma_2 + \Gamma_3 - 2\Gamma_1}{\Gamma_3 - \Gamma_2}, \tag{4}$$

$$S_{12}^{\rm PR} = S_{21}^{\rm PR} = \sqrt{\frac{2(\Gamma_3 - \Gamma_1)(\Gamma_2 - \Gamma_1)}{\Gamma_3 - \Gamma_2}}. \tag{5}$$

The S-parameters of the probe are extracted from Eqs. (3)–(5); the $S_{21}^{\rm PD}$ is provided by the manufacturer, and $S_{21}^{\rm N}$ and $S_{11}^{\rm N}$ are directly tested. So $S_{21}^{\rm EA}$ can be extracted from Eq. (2).The normalized E/O response without any terminations is plotted in Fig. 7. The extracted frequency response curve shows fluctuations in the low frequency range. This may be caused by the passive waveguide of the device. If the waveguide outside the active length has not been really passivated, the reverse voltage will be applied to it through the conductive p-doped layer on the top of it; so it will contribute to the modulation like the active waveguide at very low frequency near DC. However, microwave loss in this "passive"section

increases rapidly with increasing frequency, so its contribution to the modulation reduces rapidly at low frequency. There may be other reasons which need further consideration. A 3 dB bandwidth of 22 GHz is attained in this device. The E/O response can be further improved by flattening the response in the high-frequency regime through loading 50 Ω termination to reduce the microwave loss caused by impedance mismatch.

4. Conclusion

In summary, we have successfully fabricated a high extinction ratio and broad bandwidth EAM integrated with a passive waveguide at each side based on QWI photonic integration techniques. The DC extinction ratio is 16 dB between 0 and 4 V at 1550 nm. The cutoff 3 dB bandwidth in E/O response for the modulator is 22 GHz. The simple fabrication procedure and high performance of the device proves that it would be suitable for low-cost and mass-production external modulators for optical access networks.

Acknowledgement

The authors would like to thank Wang Baojun, Zhou Fan, Shu Huiyun for their experimental help, and Zhao Lingjuan, Wang Lufeng, Bian Jing, An Xin for their support on the device test.

References

[1] Kawanishi H, Suzuki T, Nakamura K. 1.3 μm EAM-integrated DFB lasers for 40 Gb/s very-short-reach application. Proc OFC, 2003, 1: 270

[2] Lewen R, Irmscher S, Westergren U. Segmented transmission-line electroabsorption modulators. J Lightwave Technol, 2004, 22: 172

[3] Fukano H, Yamanaka T, Tamura M, et al. 40 Gbit/s electroabsorption modulators with 1.1 V driving voltage. Electron Lett, 2004, 40: 1144

[4] Ido T, Tanaka S, Suzuki M, et al. Ultra-high-speed multiple-quantum-well electroabsorption modulators with integrated waveguides. IEEE J Lightwave Technol, 1996, 14: 2026

[5] Satzke K, Baums D, Cebulla U, et al. Ultrahigh-bandwidth (42 GHz) polarization-independent ridge waveguide electroabsorption modulator based on tensile strained InGaAsP MQW. Electron Lett, 1995, 31: 2030

[6] Kawano K, Kohtoku M, Ueki M, et al. Polarisation-insensitive travelling-wave electrode electroabsorption (TW-EA) modulator with bandwidth over 50 GHz and driving voltage less than 2 V. Electron Lett, 1997, 33: 1580

[7] Shi J W, Shiao A C, Chu C C, et al. Dual-depletion region electroabsorption modulator with evanescently coupled waveguide for high-speed (40 GHz) and low driving-voltage performance. IEEE Photonics Technol Lett, 2007, 19: 345

[8] Devaux F, Menigaux L, Brandon J, et al. Polarization-independent electroabsorption modulator integrated with spot-size converters. Proc OFC, 1996: 208

[9] Skogen E J, Raring J W, Barton J S, et al. Postgrowth control of the quantum-well band edge for the monolithic integration of widely tunable lasers and electroabsorption modulators. IEEE J Sel Topics Quantum Electron, 2003, 9: 1183

[10] Huang Y, Xia F, Menon V M, et al. Reduction of absorption loss in asymmetric twin waveguide laser tapers using argon plasma-enhanced quantum-well intermixing. IEEE Photonics Technol Lett, 2004, 16: 2221

[11] Chen J X, Wu Y, Chen W X, et al. High-power intrastep quantum well electroabsorption modulator using single-sided large optical cavity waveguide. IEEE Photonics Technol Lett, 2004, 16: 440

[12] Shin D S. Reduction in escape times of photogenerated charge carriers with asymmetric intrastep quantum well and subsequent improvement in saturation optical intensity. Jpn J Appl Phys, 2006, 45: 9063

[13] Miyazaki Y, Tada H, Tokizaki S, et al. Small-chirp 40-Gbps electroabsorption modulator with novel tensile-strained asymmetric quantum-well absorption layer. IEEE J Quantum Electrics, 2003, 39: 813

[14] Yang H, Chin M K, Zhou J, et al. A traveling-wave electroabsorption modulator with a large optical cavity and intrastep quantum wells. Semicond Sci Technol, 2008, 23: 105011

[15] Bauer G, Richter W. Optical characterization of epitaxial semiconductor layers. Berlin: Springer, 1996

[16] Aizawa T, Ravikumar K G, Suzaki S, et al. Polarization-independent quantum confined Stark effect in an InGaAs/InP tensile-strained quantum well. IEEE J Quantum Electron, 1994, 30: 585

[17] Chen Y B, Qing P J, Zhou F. High-power electroabsorption modulator using introstep quantum well. Chin Phys Lett, 2007, 24: 2128

[18] Li G L. Wide-bandwidth high-efficiency electroabsorption modulator for analog fiber-optic links. Dissertation, University of California, San Diego, 2002